Iraqi Journal of Physics, 2023 *Vol. 21 No. 4, PP. 56-65*

https://doi.org/10.30723/ijp.v21i4.1168

P-ISSN: 2070-4003
E-ISSN: 2664-5548

Structural and Magnetic Properties of $Mn_xZn_{1-x}Fe_2O_4$ Prepared via Sol-Gel Method

Nawras Kareem Ali[1a*] and Zainab Raheem Muslim[1b]

[1]*Department of Physics, College of Science, University of Baghdad, Baghdad, Iraq*

[b]E-mail: zainbraheem2018@gmail.com

[a*]Corresponding author: nouras.kareem1104a@sc,uobaghdad.edu.iq

Abstract

Manganese-zinc ferrite $Mn_xZn_{1-x}Fe_2O_4$ (MnZnF) powder was prepared using the sol-gel method. The morphological, structural, and magnetic properties of MnZnF powder were studied using X-ray diffraction (XRD), atomic force microscopy (AFM), energy dispersive X-ray (EDX), field emission-scanning electron microscopes (FE-SEM), and vibrating sample magnetometers (VSM). The XRD results showed that the MnxZn1-xFe2O4 that was formed had a trigonal crystalline structure. AFM results showed that the average diameter of Manganese-Zinc Ferrite is 55.35 nm, indicating that the sample has a nanostructure dimension. The EDX spectrum revealed the presence of transition metals (Mn, Fe, Zn, and O) in Manganese-Zinc Ferrite. The FE-SEM results of MnZnF showed uniform spherical structures. VSM was used to study the change in magnetization, the saturation magnetization, (Ms) value of the samples. The measurement of VSM indicated that the MnZnF exhibits ferromagnetic behavior with coercivity Hc (0.0014 Gauss), remanent magnetization (Mr) (0.202 emu/gr), and saturation magnetization Ms (2.69 emu/g).

Article Info.

Keywords:
$Mn_xZn_{1-x}Fe_2O_4$, XRD, AFM, FE-SEM, Magnetic Properties.

Article history:
Received: Jul. 04, 2023
Revised: Aug. 29, 2023
Accepted: Sep.11, 2023
Published:Dec.01,2023

1. Introduction

Recently, there has been a great deal of interest in studying spinel ferrite nanoparticles due to their electrical, electronic, physical, catalytic, and magnetic properties, as well as their uses in technology. The majority of spinel ferrites belong to the Fd3m space group, but some spinals have lower symmetry. Physical properties of these nano ferrites depend on the synthesis parameters such as co-precipitation time, sintering temperature and rate of heating and cooling [1-6].

Ferrites are the combination of iron oxide F and metal ions such as Li^{+3}, Zn^{+3}, Mn^{+2}, Mg^{+2}, Co^{+2}, etc. They are classified into three types: garnet, hexagonal and spinel ferrite [7]. They are also insulating magnetic oxides that exhibit high saturation magnetization, high electrical resistivity, dielectric loss with moderate permittivity and low vortex current [8, 9]. Ferrites are extremely sensitive to the preparation method, constituent metal oxide amounts, dopants or substituted elements and sintering conditions [10].

Spinel ferrite particles are a type of soft material with a structural formal (M Fe_2O_4; where M =Mg, Mn, Zn, Cu and Co). The divalent cation may belong to normal or transition elements. Two interstitial sites in the crystal structure of the spinel verities are commonly named tetrahedral (A) and octahedral (B) sites [11-13]. Ferrites are one of the most attraction and materials due to their high specific heating, low melting point, large expansion coefficient, and low magnetic transition temperature, among others [14, 15]. The structure, dielectric, magnetic, and electrical properties of nano-sized ferrites depend on the technique of preparation, sintering temperature, time, concentration, chemical composition, and distribution of the cations between the tetrahedral (A) and octahedral (B) sites [16, 17].

Manganese-Zinc ferrites ($Mn_xZn_{x-1}Fe_2O_4$) have spinel structure [18]. The unit cell of spinel ferrite is FCC, with 8 formula units per unit cell, having 64 tetrahedral

sites surrounded by 4 oxygen atoms and 32 octahedral sites, surrounded by six oxygen atoms [19, 20]. In the Mn-Zn spinel ferrite lattice, Zn ions are on the tetrahedral sites, while iron and manganese ions occupy both tetrahedral and octahedral positions [21].

$Mn_xZn_{x-1}Fe_2O_4$ are preferred due to thier high magnetic induction, high permeability, low power losses, and saturation induction [22]. They are of great interest due to their wide range of applications, such as high-frequency [23], magnetic fluid [24], biomedicines [25], magnetic resonance [26], and catalysis [27].

Ferrites can be prepared by a large number of chemical and physical techniques that have been applied by scientists all over the world for the synthesis of ferrites, such as co-precitation [28], sol-gel [29], solid state reaction [30], hydrothermal [31], microemulsion [32],and combustion techniques [33]. Sol-gel technique, which is both cost effective and environmentally friendly, has been used to synthesize magnetic ferrite particles [34, 35].

Ferrites exhibit applications in wide-range fields, including electrode material for supercapacitors [36], photocatalytic activity [37], biomedical [38], sensors and biosensors [39, 40], photoelectric devices [41], and magnetic pigments [42]. Spinel ferrites have received interest in numerous biomedical applications due to their bio-friendliness, lower toxicity than other metal ferrites, chemical stability, simple and reproducible manufacturing and low saturation magnetization [43, 44]. In this study, the manganese-Zinc ferrite was prepared using the sol-gel technique, and studied their morphological, structural and magnetic properties were investigated using XRD, AFM, EDX, FE-SEM and VSM.

2. Experimental Part

2.1. Raw Materials

The following raw materials were used in the preparation of the sample: zinc nitrate $ZnNO_3$ with a purity of 98%; manganese nitrate $MnNO_3$ with a purity of 99.9%; citric acid ($C_6H_8O_7$) with a purity of 99%; and ferric nitrate (Fe (NO_3)$2.9H_2O$) with a purity of 99 %.

2.2. Preparation of Manganese-Zinc Ferrites $Mn_xZn_{1-x}Fe_2O_4$

$Mn_{0.5}Zn_{0.5}Fe_2O_4$ composite was prepared by the chemical sol-gel method. The materials used to prepare $Mn_{0.5}Zn_{0.5}Fe_2O_4$, nitrates (manganese, zinc and iron) were mixed with deionized water 30 ml, and citric acid in a ratio of (1:1:1:3). The mixture was heated under stirring to 70 °C for 5 hr to make the mixture denser where the gel formed. The gel was oven-dried at 150 °C for 6 hr and grinded to form powder. Then the beaker was placed in a furnace for 6 hr at 700 °C to eliminate the organic residues in the gel. Fig. 1 shows the schematic diagram of preparation of the MnZnF powder using the sol-gel method.

2.3. Characterization of Materials

2.3.1 X- Ray Diffractometer

X-ray diffractometer (XRD) (Shimadzu-6000, Japan) with cu-kα radiation (k=1.54056A°) was used for phase identification of the prepared samples.

2.3.2 Atomic Force Microscopy

Atomic Force Microscopy (AFM) (Angstrom TT-2AFM, USA) was used to measure the average diameter and roughness of surface of the sample in the powder shape.

2.3.3 Energy Dispersive X-Ray

The chemical composition was evaluated using an energy dispersive X-ray spectrometer (EDX) in Taban Lab, department of physics, University of Tehran.

2.3.4 Field Emission Scanning Electron Microscope

The microstructure of the powder was observed using field emission scanning electron microscope (FE-SEM) model (Inspect 50 FE-SEM) in Taban Lab, department of physics, University of Tehran.

2.3.5 Vibration Sample Magnetometer

A vibration sample magnetometer (VSM) (Daypetronic Company, 021-26651864) was used to determine the magnetic characteristics of the samples. These measurements were done at room temperature in Taban Lab, department of Physics, University of Tehran, to detect magnetization against applied field with a magnetic field of -8kOe ≤ H ≤ 8kOe.

3. Results and Discussion

3.1. X-ray Diffraction for Manganese-Zinc Ferrite ($Mn_xZn_{1-x}Fe_2O_4$)

The X-ray diffraction spectra of manganese-zinc ferrite synthesized using the sol-gel method is shown in Fig. 1. The X-ray spectra indicate trigonal structure of $Mn_xZn_{1-x}Fe_2O_4$ with card (JCPDS NO. 96-901-3530), and the second phase Hematite Fe_2O_3 has trigonal structure with card (JCPDS No. 96-900-9783). The main peaks at 18.2184, 29.9713, 35.2874, 36.8678, 42.9023, 53.2471, 56.7529, 62.3276, 70.7759, and 73.5920 correspond to (111), (220), (222), (311), (400), (422), (511), (440), (620) and (533) indicate the formation of pure $Mn_xZn_{1-x}Fe_2O_4$. Some extra secondary peaks (Hematite Fe_2O_3 secondary phases) were seen adjacent to characteristics peak and perhaps due to the impurity phase. The formation of the impurity phase of hematite during calcination at 700°C could be due to hematite is thermally stable at a high annealing temperature. This agrees with the result obtained by [45]. Table 1 lists the structural properties (index plan, FWHM, and grain size).

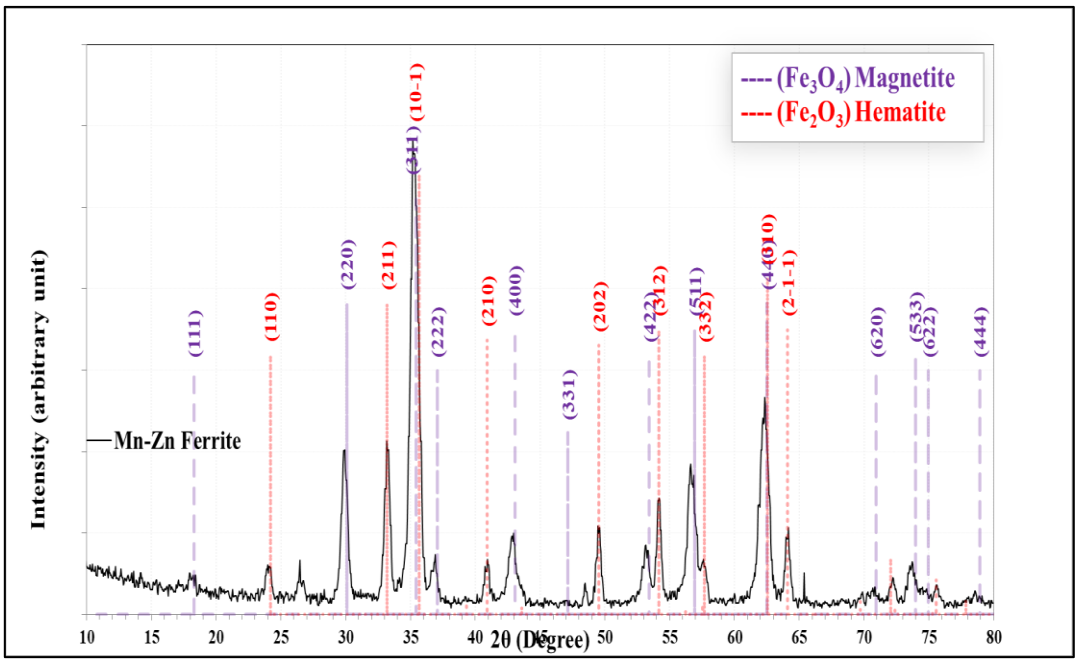

Figure 1: XRD spectra of $Mn_xZn_{1-x}Fe_2O_4$.

Table 1: The structural properties of MnZnF.

Sample	2θ (Deg.)	FWHM (Deg.)	d_{hkl} Exp.(Å)	G.S (nm)	hkl	Phase	Card No.
Mn-Zn Ferrite	18.2759	0.6896	4.8504	11.7	(111)	Magnetite	96-901-3530
	24.0517	0.5747	3.6971	14.1	(110)	Hematite	96-900-9783
	29.8563	0.6034	2.9902	13.6	(220)	Magnetite	96-901-3530
	33.2184	0.4885	2.6948	17.0	(211)	Hematite	96-900-9783
	35.2299	0.6896	2.5454	12.1	(311)	Magnetite	96-901-3530
	36.9253	0.4310	2.4324	19.4	(220)	Magnetite	96-901-3530
	40.9195	0.4886	2.2037	17.4	(210)	Hematite	96-900-9783
	42.8448	0.5460	2.1090	15.6	(400)	Magnetite	96-901-3530
	49.5690	0.4310	1.8375	20.3	(202)	Hematite	96-900-9783
	53.1609	0.4885	1.7215	18.2	(422)	Magnetite	96-901-3530
	54.1954	0.4311	1.6911	20.7	(312)	Hematite	96-900-9783
	56.6379	0.6322	1.6238	14.3	(511)	Magnetite	96-901-3530
	57.6437	0.4885	1.5978	18.6	(332)	Hematite	96-900-9783
	62.3276	0.7758	1.4885	12.0	(440)	Magnetite	96-901-3530
	64.1379	0.4023	1.4508	23.3	(2-1-1)	Hematite	96-900-9783
	70.7759	0.5173	1.3301	18.8	(620)	Magnetite	96-901-3530
	73.7069	0.6610	1.2843	15.0	(533)	Magnetite	96-901-3530

3.2 Atomic force microscopy of ($Mn_xZn_{1-x}Fe_2O_4$)

The AFM images of the surface of the MnZnF are shown in Figs.2 (a and b). The images show a uniform surface, indicating that the particle has uniform dimensions. Fig.2(a) shows the 2D image of the sample, while Fig.2(b) shows 3D image that shows an exaggeration of the Z range to display the characteristics of the sample. The average diameter of the surface of MnZnF is 55.35 nm, which indicates nanostructure dimensions of these samples.

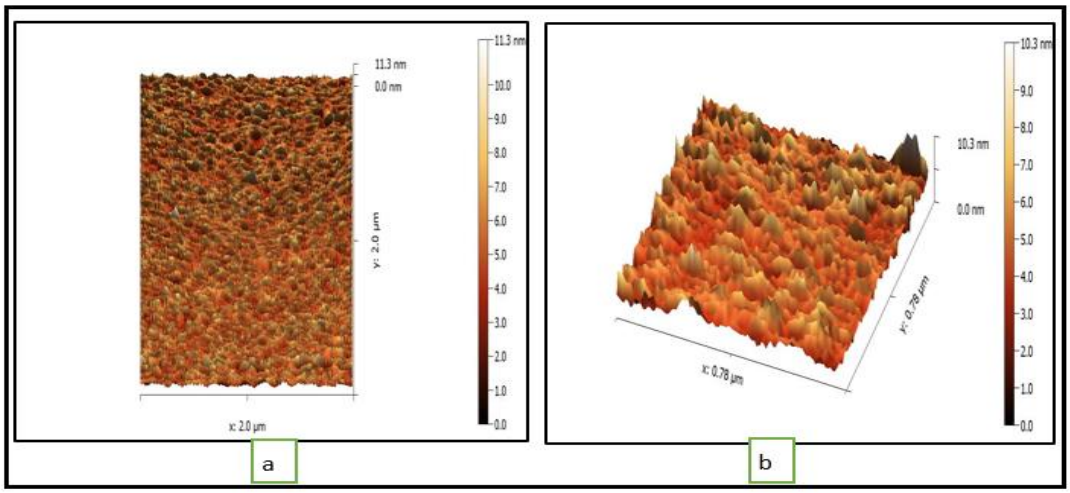

Figure 2: AFM of $Mn_xZn_{1-x}Fe_2O_4$ a) 2D, b) 3D.

The grain analysis revealed that there are 67 different particles that can be studied (Fig. 3(a)). From the histogram in Fig. 3(b), it was noticed that a large number of heights fall in the 64 to 75 nm tall category. From the table in Fig. 3(c), the root mean

square roughness (Sq) is 7.579 nm. Additionally, this table shows the highest peak (Sp) of the sample in Z, which is 17.17nm.

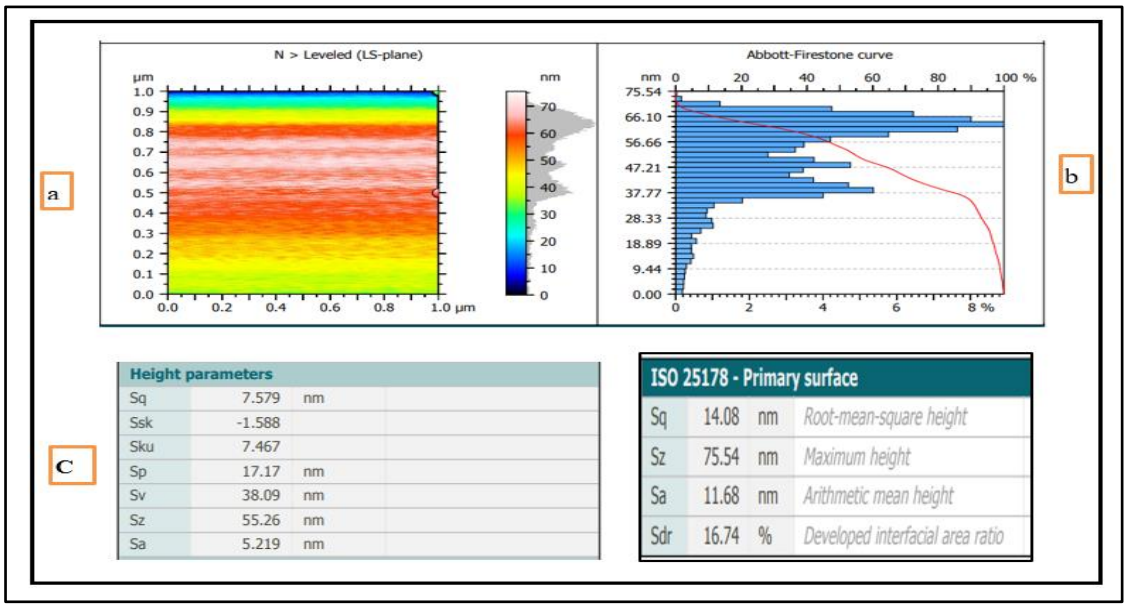

Figure 3: (a) Roughness analysis in the image of MnZnF, (b) Histogram analysis in the image of (a), (c) Grain analysis in the image (a).

3.3. Energy Dispersive X-Ray of ($Mn_xZn_{1-x}Fe_2O_4$)

The corresponding EDX spectrum was studied to determine the elemental composition on the surface of MnZnF powder. Fig. 4 displays the EDX of the peaks of (Mn, Zn, Fe and O) elements for MnZnF powder. The spectrum of the manganese-zinc ferrite can show the highest intensity of iron (Fe). The small peak at 2.1 KeV indicates the presence of Au (gold), which was utilized as a sputter coating during sample production. The atomic ratio of Fe:Zn:Mn:O was discovered to be (23.04:10.10:10.34:56.52).

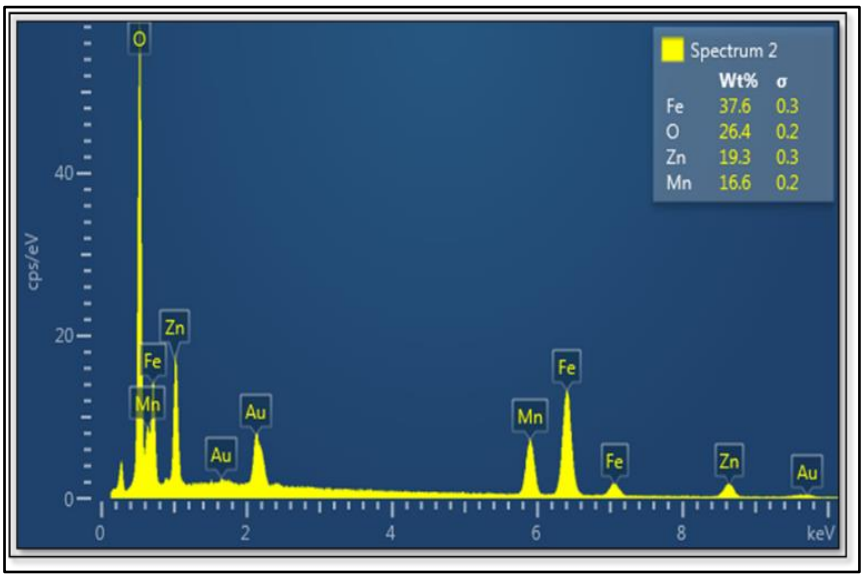

Figure 4: EDX of $Mn_xZn_{1-x}Fe_2O_4$.

3.4. Field Emission Scanning Electron Microscope of $Mn_xZn_{1-x}Fe_2O_4$

High-resolution FE-SEM images of the manganese-zinc ferrite (MnZnF) powder calcined at 700 °C for 5 hr are shown in Fig. 5 (a, b); The FE-SEM images indicate that

the sample consisted of well-crystallized homogenous particles, most of which are spherical in shape and smooth on the surface.

FE-SEM images for MnZnF at different magnifications are shown in Fig. 5(c). The surface morphology of MnZnF was characterized by particle distribution at different sizes with grain boundaries of a spherical shape. It is also worth noting that the faceted crystals can also be observed. D1 (58.34 nm) and D2 (75.83 nm) are shown in Fig. 5(c).

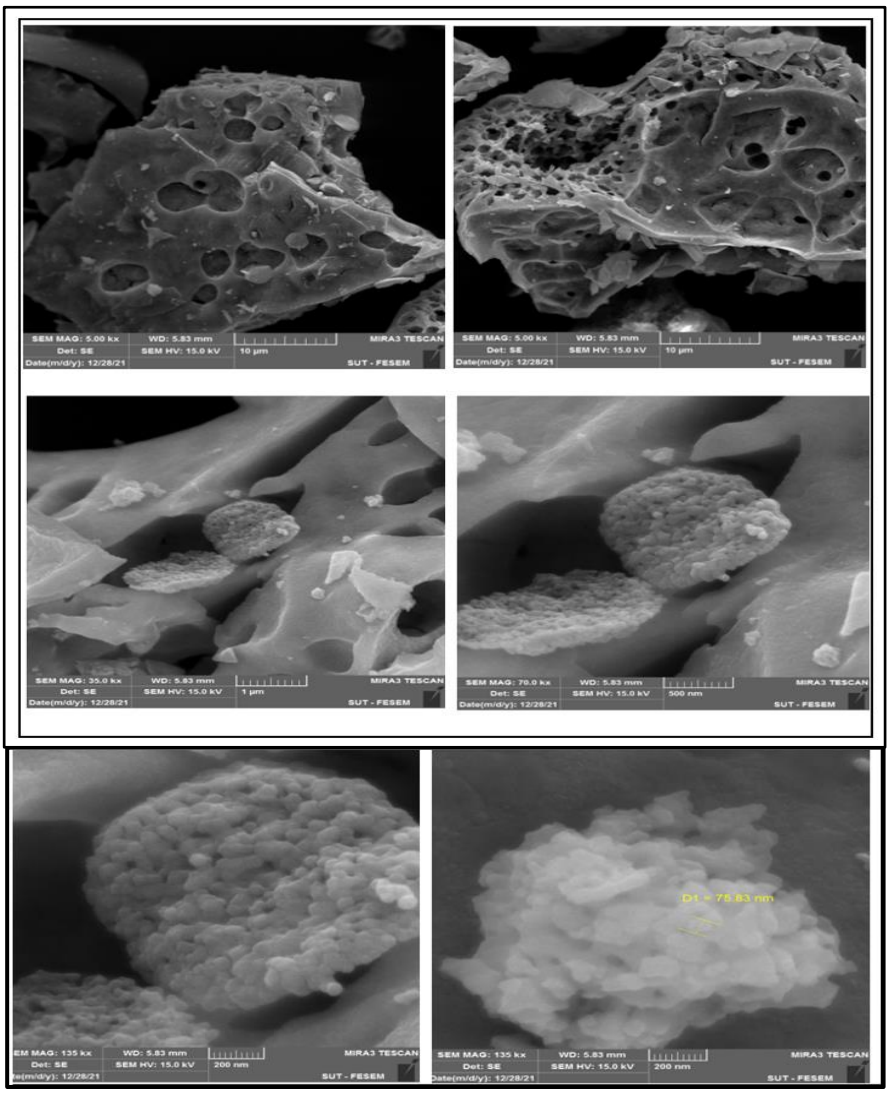

Figure 5: (a, b, and c) FE-SEM images of $Mn_xZn_{1-x}Fe_2O_4$.

3.5. Magnetic Properties of $Mn_xZn_{1-x}Fe_2O_4$

Magnetization against applied field was measured using a VSM with a magnetic field of -10kOe ≤ H ≤ 10kOe. The saturation magnetization (Ms), remanent magnetization (Mr), and coercivity (Hc) values were estimated using the hysteresis curve shown in Fig. 6, and the results are shown in Table 2. Magnetic characteristics are often controlled by the exchange interaction of metallic ions on the two interacting sub-lattices A and B.

Fig. 6 shows the hysteresis loops for $Mn_xZn_{1-x}Fe_2O_4$, indicating the existence of ferromagnetism. These loops are due to the increase in the magnetic nature (5 μB) of the Mn^{+2} concentration [46]. The variation in cation sharing between the A- and B- sites is probably what caused the change in the value of Ms. Mn^{+2} ions have a tendency to enter the B-sites in the crystal lattice. On the other hand, Zn^{+2} ions have a preference for the

A-site, due to their readiness to form covalent bonds involving sp3 hybrid orbitals [47]. However, the non- magnetic Zn^{+2} (0 μB) is replaced by the magnetic Mn^{+2} (5 μB) ions, increasing the Ms when the magnetic Mn^{+2} ions begin to occupy the B-sites and displace the Fe^{+3} ions from the B-sites, which then begin to migrate towards the A-sites. Fe^{+3} ions thus partially occupy the A- and B- sites [48].

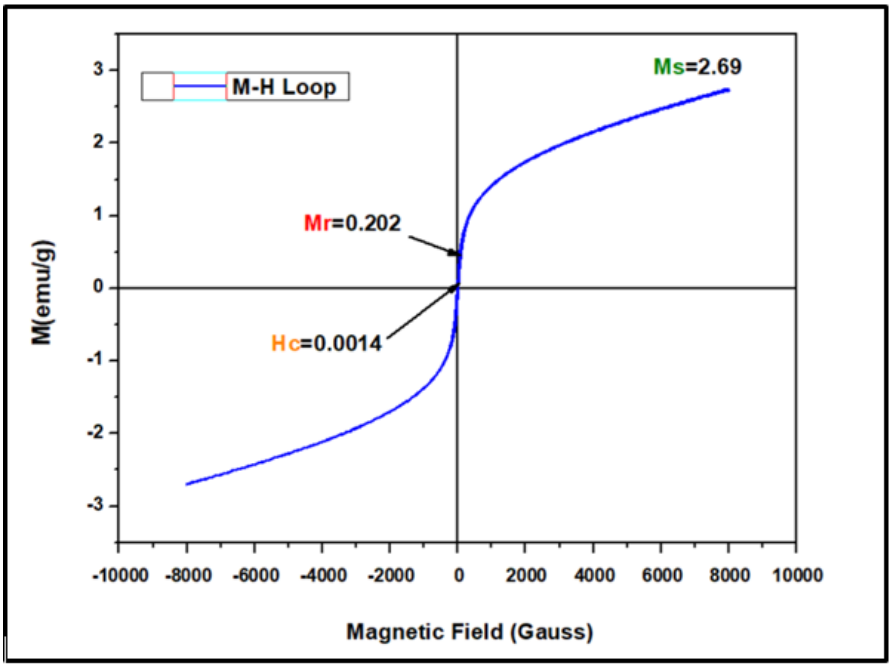

Figure 6: Magnetization versus applied field for $Mn_xZn_{1-x}Fe_2O_4$.

Table 2: The magnetic properties of MnZnF ferrite.

Magnetic parameters	Ms (emu/g)	Mr (emu/g)	Mc (Oe)
$Mn_xZn_{1-x}Fe_2O_4$	2.69	0.202	0.0014

Decrease in H_c values is because Mn^{+2} has less magnetocrystalline anisotropy than Zn^{+2}. The magnetic properties of ferrite nanoparticles are strongly influenced by their composition and cation distribution at octahedral and tetrahedral sites [49]. In a ferromagnetic spinel structure, super-exchange interactions between the metal ions in the tetrahedral (A) and octahedral (B) sublattices create the magnetic order. As a result, changing the cations can change the samples' magnetic characteristics.The saturation magnetization was decreased as a result of the Fe moving to the A site. This may be due to the weakening of the exchange between (A) and (B) sites [50].

4. Conclusions

The structural and magnetic properties of $Mn_xZn_{1-x}Fe_2O_4$ powder were prepared using the Sol-Gel method. The XRD found a trigonal structure for MnZnF. FE-SEM and AFM analyses were used to examine the morphology and average diameter of Manganese-Zinc Ferrite. The EDX spectrum indicates the presence of transition metals (Mn, Zn, Fe, and O). VSM was used to evaluate the magnetic characteristics of $Mn_xZn_{x-1}Fe_2O_4$. The measurement indicates that the MnZnF exhibits ferromagnetic behavior with coercivity Hc (0.0014 Gauss), remanence Mr (0.202 emu/g), and saturation magnetization Ms (2.69 emu/g).

Acknowledgements

The authors gratefully acknowledge to the material lab in Department of Physics, College of Science, University of Baghdad.

Conflict of Interest

Authors declare that they have no conflict of interest.

References

1. D. R. Kumar, C. A. Lincoln, D. Ravinder, and S. I. Ahmad, Appl. Phys. A **126**, 705 (2020).
2. M. M. Ismail and N. A. Jaber, Iraqi J. Phys. **16**, 140 (2018).
3. A. Mary Jacintha, A. Manikandan, K. Chinnaraj, S. Arul Antony, and P. Neeraja, J. Nanosci. Nanotech. **15**, 9732 (2015).
4. S. K. Pendyala, K. Thyagarajan, A. Gurusampath Kumar, and L. Obulapathi, J. Aust. Ceramic Soci. **54**, 467 (2018).
5. M. F. Al-Hilli, Iraqi J. Sci. **57**, 2245 (2016).
6. M. Chand, A. Kumar, S. Kumar, A. Shankar, and R. Pant, Indian J. Eng. Mat. Sci. **18**, 385 (2011).
7. L. Thakur and B. Singh, Integ. Res. Advan. **1**, 11 (2014).
8. R. K. Panda, Doctor of Philosophy Thesis, National Institute of Technology, 2016.
9. E. C. Abenojar, S. Wickramasinghe, J. Bas-Concepcion, and A. C. S. Samia, Prog. Nat. Sci. Mat. Int. **26**, 440 (2016).
10. P. Tehranian, A. Shokuhfar, and H. Bakhshi, J. Supercond. Nov. Magnet. **32**, 1013 (2019).
11. A. M. Hammeed and Z. R. Muslim, in IOP Conference Series: Materials Science and Engineering (IOP Publishing, 2020). p. 072019.
12. M. a. A. Al-Karboli, S. a. H. Al-Dabbagh, and R. M. S. Al-Alwany, Iraqi J. Phys. **16**, 79 (2018).
13. L. Phor, S. Chahal, and V. Kumar, J. Advan. Ceram. **9**, 576 (2020).
14. S. Shamebo and E. Arbaminch, MSc Thesis, Arba Minch,
15. T. Dippong, E. A. Levei, and O. Cadar, Nanomaterials **11**, 1560 (2021).
16. Z. S. Sadeq, Iraqi J. Sci. **63**, 997 (2022).
17. K. Maaz, J. Duan, S. Karim, Y. Chen, P. Zhai, L. Xu, H. Yao, and J. Liu, J. All. Comp. **684**, 656 (2016).
18. S. Sanatombi, S. Sumitra, and S. Ibetombi, Iranian J. Sci. Tech. Trans. A: Sci. **42**, 2397 (2018).
19. B. K. Mohammed, Iraqi J. Sci. **58**, 848 (2017).
20. N. Matsushita, K. Kondo, S. Yoshida, M. Tada, M. Yoshimura, and M. Abe, J. Electroceram. **16**, 557 (2006).
21. M. Li, H. Fang, H. Li, Y. Zhao, T. Li, H. Pang, J. Tang, and X. Liu, J. Supercond. Novel Magnet. **30**, 2275 (2017).
22. H. Sharouf and Z. Saffour, Baghdad Sci. J., 1 (2023).
23. G. Kogias and V. Zaspalis, Ceram. Int. **42**, 7639 (2016).
24. P. Andalib, Y. Chen, and V. G. Harris, IEEE Magnet. Lett. **9**, 1 (2017).
25. M. Latorre-Esteves, A. Cortes, M. Torres-Lugo, and C. Rinaldi, J. Magnet. Magnet. Mat. **321**, 3061 (2009).
26. Y. Ying, Y. Gong, D. Liu, W. Li, J. Yu, L. Jiang, and S. Che, J. Supercond. Novel Magnet. **30**, 2129 (2017).
27. D. H. K. Reddy and Y.-S. Yun, Coord. Chem. Rev. **315**, 90 (2016).
28. J. Stergar, Z. Jirák, P. Veverka, L. Kubíčková, T. Vrba, J. Kuličková, K. Knížek, F. Porcher, J. Kohout, and O. Kaman, J. Magnet. Magnet. Mat. **475**, 429 (2019).

29. R. F. Kadhim and Z. R. Muslim, in Journal of Physics: Conference Series (IOP Publishing, 2020). p. 012003.
30. M. Abbas and M. Rasheed, in Journal of Physics: Conference Series (IOP Publishing, 2021). p. 012059.
31. F. A. Mutlak, Iraqi J. Phys. **17**, 10 (2019).
32. A. Košak, D. Makovec, A. Žnidaršič, and M. Drofenik, J. European Ceram. Soci. **24**, 959 (2004).
33. J. Feng, R. Xiong, Y. Liu, F. Su, and X. Zhang, J. Mat. Sci. Mat. Elect. **29**, 18358 (2018).
34. K. Rotjanasuworapong, W. Lerdwijitjarud, and A. Sirivat, Nanomaterials **11**, 876 (2021).
35. I. M. Obaidat, B. Issa, and Y. Haik, Nanomaterials **5**, 63 (2015).
36. E. Mazarío, A. Mayoral, E. Salas, N. Menéndez, P. Herrasti, and J. Sánchez-Marcos, Mat. Des. **111**, 646 (2016).
37. R. F. Kadhim, Iraqi J. Phys. **15**, 11 (2017).
38. R. M. Ahmed, S. S. A. Rahman, D. H. Badri, K. M. Sultan, I. Y. Majeed, and G. M. Kamil, Baghdad Sci. J., 1 (2023).
39. F. Falsafi, B. Hashemi, A. Mirzaei, E. Fazio, F. Neri, N. Donato, S. G. Leonardi, and G. Neri, Ceram. Int. **43**, 1029 (2017).
40. I. Sandu, L. Presmanes, P. Alphonse, and P. Tailhades, Thin Sol. Fil. **495**, 130 (2006).
41. K. Nejati and R. Zabihi, Chem. Cen. J. **6**, 1 (2012).
42. E. A. Ajaj, Z. R. Musleem, and B. M. Al-Shabander, Iraqi J. Phys. **13**, 171 (2015).
43. R. Sharma, S. Bansal, and S. Singhal, RSC Advan. **5**, 6006 (2015).
44. T. Guo, M. Lin, J. Huang, C. Zhou, W. Tian, H. Yu, X. Jiang, J. Ye, Y. Shi, Y. Xiao, X. Bian, and X. Feng, J. Nanomat. **2018**, 7805147 (2018).
45. A. Hakeem, T. Alshahrani, G. Muhammad, M. Alhossainy, A. Laref, A. R. Khan, I. Ali, H. M. T. Farid, T. Ghrib, and S. R. Ejaz, J. Mat. Res. Tech. **11**, 158 (2021).
46. U. S. Sharma and R. Shah, in AIP Conference Proceedings (AIP Publishing, 2020). p.
47. C. Anumol, M. Chithra, S. Rout, and S. C. Sahoo, J. Supercond. Novel Magnet. **33**, 1611 (2020).
48. H. Moradmard, S. F. Shayesteh, P. Tohidi, Z. Abbas, and M. Khaleghi, J. All. Comp. **650**, 116 (2015).
49. C. Choodamani, B. Rudraswamy, and G. Chandrappa, Ceram. Int. **42**, 10565 (2016).
50. R. Ramzan, M. Tariq, M. N. Ashiq, H. Albalawi, I. Ahmad, M. Alhossainy, S. R. Ejaz, R. Y. Khosa, H. M. T. Farid, and H. M. Khan, J. Mat. Res. Tech. **12**, 1104 (2021).

الخصائص التركيبية والمغناطسية $Mn_xZn_{1-x}Fe_2O_4$ المحضرة بطريقة سول-جل

نورس كريم علي[1] و زينب رحيم مسلم[1]
[1] قسم الفيزياء، كلية العلوم، جامعة بغداد، بغداد، العراق

الخلاصة

تم تحضير مسحوق فيرايت المنغنيز -الزنك ($Mn_xZn_{1-x}Fe_2O_4$) باستخدام طريقة السول-جل. وتم دراسة الخصائص التركيبة والمغناطيسية لمسحوق (MnZnF) باستخدام XRD و AFM و EDX و FE-SEM و VSM. اظهرت النتائج حيود الأشعة السينية (XRD) تكوين التركيب الثلاثي البلوري لمسحوق $Mn_xZn_{1-x}Fe_2O_4$. اظهرت نتائج الفحص المجهري للقوة الذرية (AFM) بان معدل قطر للفرايت المنغنيز -الزنك هوبحدود (55.35 نانومتر)، وهذا يشير إلى أن النموذج لها أبعاد نانوية. يظهر طيف الأشعة السينية المشتتة للطاقة (EDX) وجود معادن الانتقالية (المنغنيز، الزنك، الحديد، لاوكسجين) للفرايت المنغنيز الزنك. من خلال المسح المجهر الإلكتروني لمسح الانبعاث (FE-SEM) لـ MnZnF لوحظ بان التركيب يحتوئ على جزيئات كروية. وتم استخدام VSM لدراسة التغير في M_s وحساب الخصائص المغناطسية ل MnZnF. باستخدام مقياس المغناطسية (VSM) وتشير الحسابات بان MnZnF لة تصرف مغناطيسي حديدي ذو قوة قهرية هي (0.0014 Gauss) وقيمة مغناطسية المتبقية (M_r) هي (0.202emu/g) وقيمة الثبات المغناطيسي (M_s) هي (2.69emu/g).

الكلمات المفتاحية: فريت المنغنيز-الزنك، حيود الاشعة السينية، الفحص مجهري للقوة الذرية، المسح المجهر الالكتروني، الخواص المغناطسية.